



The Physical Parameters of Clumps Associated with Class I Methanol Masers

Dmitry A. Ladeyschikov¹ , James S. Urquhart² , Andrey M. Sobolev¹, Shari L. Breen³ , and Olga S. Bayandina⁴ 

¹Ural Federal University 51 Lenin Str., 620051 Ekaterinburg, Russia; dmitry.ladeyschikov@urfu.ru

²Centre for Astrophysics and Planetary Science, University of Kent, Canterbury CT2 7NH, UK

³SKA Organisation, Jodrell Bank Observatory, SK11 9DL, UK

⁴Joint Institute for VLBI ERIC Oude Hoogeveensedijk 4, 7991 PD Dwingeloo, The Netherlands

Received 2020 March 25; revised 2020 September 8; accepted 2020 September 9; published 2020 October 20

Abstract

We present a study of the association between class I methanol masers and cold dust clumps from the APEX Telescope Large Area Survey of the Galaxy (ATLASGAL) survey. It was found that almost 100% of class I methanol masers are associated with objects listed in the ATLASGAL compact source catalog. We find a statistically significant difference in the flux density, luminosity, number and column density, and temperature distributions of ATLASGAL sources associated with 95/44 GHz methanol masers compared with those ATLASGAL sources devoid of 95 GHz methanol masers. The masers tend to arise in clumps with higher densities, luminosities, and temperatures compared with both the full sample of ATLASGAL clumps, as well as the sample of ATLASGAL sources that were cross-matched with positions previously searched for methanol masers but with no detections. Comparison between the peak position of ATLASGAL clumps and the interferometric positions of the associated class I and II methanol masers reveals that class I masers are generally located at larger physical distances from the peak submillimeter emission than class II masers. We conclude that the tight association between ATLASGAL sources and class I methanol masers may be used as a link toward understanding the conditions of the pumping of these masers and evolutionary stages at which they appear.

Unified Astronomy Thesaurus concepts: [Astrophysical masers \(103\)](#); [Interstellar medium \(847\)](#); [Astronomy databases \(83\)](#); [Dust continuum emission \(412\)](#)

1. Introduction

Methanol masers are ubiquitous features of shock waves and star formation regions (SFRs) in both our own and other galaxies. On the basis of the works of Batrla et al. (1987) and Menten (1991) methanol masers are divided into two classes—I and II. Class II methanol masers (MMII) have a radiative–radiative (source–sink notation) pumping mechanism (Cragg et al. 2005) and are usually found close to the sources of strong radiation. MMII are associated with high-mass SFRs (e.g. Billington et al. 2019). Class I methanol masers (MMI) have a collisional–radiative pumping mechanism (Sobolev et al. 2007) and are usually found at some distance from a radiation source—in the shock waves that produce suitable conditions to excite these masers. Unlike MMII, MMI trace not only high-mass SFRs but also low-mass SFRs (Kalenskii et al. 2013) and other sites with shock waves, including supernova remnants (Pihlström et al. 2014), molecular cloud collisions (Salii et al. 2002), and H II regions interacting with molecular gas (Voronkov et al. 2010). Association with the shocked regions implies that MMI are produced in the regions where densities and temperatures are elevated. This is in good agreement with results of model calculations (Voronkov et al. 2006; Leurini & Menten 2018; Sobolev & Parfenov 2018).

Submillimeter continuum emission directly probes the dense interstellar material from which stars form and therefore where MMI may appear. The APEX Telescope Large Area Survey of the Galaxy (ATLASGAL) 870 μm survey (Schuller et al. 2009) produced a large-scale, systematic database of massive pre- and protostellar clumps in the Galaxy. This survey reveals the location of the highest density regions in the interstellar medium. Recently Ladeyschikov et al. (2019) compiled a database of all the known MMI, providing an opportunity for comparison between the location of these masers with the dust continuum emission at 870 μm .

Comparison between MMII and ATLASGAL 870 μm emission was previously made in Urquhart et al. (2013, 2015) and Billington et al. (2019). In each of these papers an association was found between 99% of MMII detected in the Methanol MultiBeam (MMB) survey (Caswell et al. 2010, 2011; Green et al. 2010, 2012; Breen et al. 2015), with compact, dense clumps from the ATLASGAL catalog (Contreras et al. 2013; Urquhart et al. 2014a). The MMB source sample was matched to ATLASGAL in the range of $280^\circ < l < 20^\circ$ in Urquhart et al. (2013). In Urquhart et al. (2015) a dedicated program of follow-up Atacama Pathfinder EXperiment (APEX) observations of ~ 70 MMB sources was presented. Data from the final part of the MMB catalog ($20^\circ < l < 60^\circ$; Breen et al. 2015), which was not available on the time of publication of Urquhart et al. (2013, 2015), was analyzed in Billington et al. (2019), where the authors identified the host clumps for 958 MMII across the Galactic plane and studied their physical parameters using a combination of ATLASGAL and the James Clerk Maxwell Telescope (JCMT) Plane Survey catalogs (JPS; Moore et al. 2015; Eden et al. 2017).

The relationship between MMI and cold dust clumps was previously studied by Chen et al. (2012). The authors conducted a 95 GHz MMI survey toward color-selected Galactic Legacy Infrared Midplane Extraordinaire (GLIMPSE) sources associated with Bolocam 1.1 mm cold dust clumps (Aguirre et al. 2011; Dunham et al. 2011). It was reported that clumps associated with MMI had higher values of column density and integrated flux density.

In this paper, we compare the full sample of known MMI from the maser database (Ladeyschikov et al. 2019) with the data from the ATLASGAL survey of cold dust clumps at 870 μm . We used the following transitions of MMI for matching with the ATLASGAL survey: 95, 84, 44, and 36 GHz. We used the

observations from more than 100 papers, but the following papers make the most significant contribution to the statistics: Yang et al. (2017, 2020), Kim et al. (2018, 2019), Chen et al. (2011, 2012), Gan et al. (2013), Bae et al. (2011), Breen et al. (2019), Jordan et al. (2015, 2017), and Val'tts et al. (2020). The full list of papers incorporated into the class I maser database and used for analysis in this paper is available online.⁵

Cross-matching between MMI and dust clumps in the central molecular zone (CMZ) was not considered in this paper, as the masers in this region (such as those detected by Cotton & Yusef-Zadeh 2016) are much more crowded and numerous compared to other parts of the Galactic plane. Other methods and techniques need to be applied to study the association between MMI and dust clumps in this region; the detailed analysis of this region will be presented in a future publication.

2. Data Processing

2.1. Source Sample: MMI and Cold Dust Emission

The class I maser database (Ladeyschikov et al. 2019) was used to combine the Galactic distribution of all published MMI observations (single-dish or interferometric) into maser sites. The details of the grouping process for these methanol masers are presented in Section 2.6 of Ladeyschikov et al. (2019). In some instances maser sites have been observed on more than one occasion using different facilities. In our analysis we adopt flux densities measured with single-dish telescopes and where available we use positions derived from interferometric observations to determine the angular separation between MMI and ATLASGAL sources. In a case where there is more than one positional measurement for a particular maser available, the median value is used. In a case where more than one measurement of the flux density is available, the maximum value is used. The subsequent analysis in the paper was performed on maser sites, not on the individual maser observations.

The ATLASGAL 870 μm survey (Schuller et al. 2009), obtained using the APEX telescope, is a continuum survey covering the whole inner Galactic plane ($280^\circ < l < 60^\circ$, $|b| < 1.5^\circ$). The ATLASGAL catalog (Contreras et al. 2013; Urquhart et al. 2014a) consists of 10163 sources, including 517 that are located in the CMZ ($359.3 < l < 1.7$, $|b| < 0.2$). This catalog was produced using the source extraction algorithm SExtractor (Bertin & Arnouts 1996) and is 99% complete at $\sim 6\sigma$, which corresponds to a 870 μm peak flux density of 0.3–0.4 Jy beam⁻¹, and has a positional accuracy of $\sim 4''$ (Contreras et al. 2013; Urquhart et al. 2014a). The physical properties (distance, dust temperature, luminosity, mass, and gas column density) have been determined for approximately 8000 of these dense clumps (Urquhart et al. 2018). Matching the methanol maser samples with these dense clumps provides a straightforward and convenient way of investigating the physical conditions from which these masers arise.

The maser database presented in Ladeyschikov et al. (2019) contains 532 masers located in the ATLASGAL region studied in this paper ($280^\circ < l < 60^\circ$, $|b| < 1.5^\circ$) excluding ~ 2000 of 36 GHz maser located in the CMZ (Cotton & Yusef-Zadeh 2016). The number of masers detected within the region at 95 GHz is 420, at 44 GHz is 355, at 84 GHz is 83, and at 36 GHz is 95. There is some overlap between objects observed

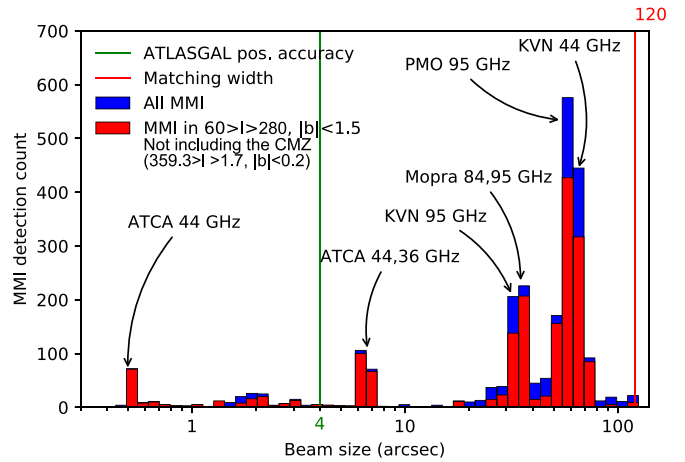


Figure 1. Log-based histogram of primary beam sizes of MMI observations in the studied sample. Blue bars refer to the whole MMI database. Red bars show masers in the currently studied sample ($280^\circ < l < 60^\circ$, $|b| < 1.5^\circ$). The green vertical line indicates ATLASGAL positional accuracy ($4''$). The red vertical line shows the matching threshold for the association between MMI and ATLASGAL clumps. Labels mark the facilities that make the most significant contributions to the histogram.

at different frequencies: the number of objects detected at both 95 and 44 GHz is 253, and 69 sources are detected at all of the frequencies considered.

2.2. Catalog Cross-matching

The cross-matching between MMI and ATLASGAL catalogs was done in two independent ways.

First we looked for matches between the maser sites and ATLASGAL clumps by determining the positional offsets in arcsecs from their catalog positions, and comparing this to the matching radius; we consider masers and dust clumps to be physically associated if the angular offset is smaller than the matched radius, while pairs with larger offsets are discarded. If more than one ATLASGAL clump is matched to a particular maser, then the clump with the smallest angular offset to the MMI center is considered to be the most likely association.

The matching radius depends mainly on the maximum beam size of maser observations and this can vary significantly due to the large range of beam sizes of the studies used to produce the maser database (see Figure 1 for telescope beam sizes). There are ~ 440 MMI detections with high accuracy positions (synthesized beam size $0''.4\text{--}7''$) derived from the Very Large Array (VLA), Australia Telescope Compact Array (ATCA), Atacama Large Millimeter/submillimeter Array (ALMA), and Submillimeter Array (SMA) interferometers. However, the number of single-dish observations with detections (~ 2000 ; 82% of all detections) dominates over the number of available interferometric observations. The beam size of single-dish detections varies from $10''$ (IRAM 30 m at 229 GHz), $55''$ (Mopra 22 m at 95 GHz) to $105''$ (Onsala 20 m at 36 GHz). An analysis of the beam size distribution of the combined sample (see Figure 1) suggests that a matching radius of $60''$, corresponding to a beam FWHM of $120''$, covers almost all maser observations. Thus we use a matching radii of $60''$ in all subsequent analyses.

In addition to the source catalog, SExtractor also produced image masks marking the location and extent of each extracted clump. In these masks the flux values for each clump have been replaced with an integer value that links the pixels associated with each clump to their catalog entry. Converting the maser

⁵ <http://maserdb.net/list.pl>

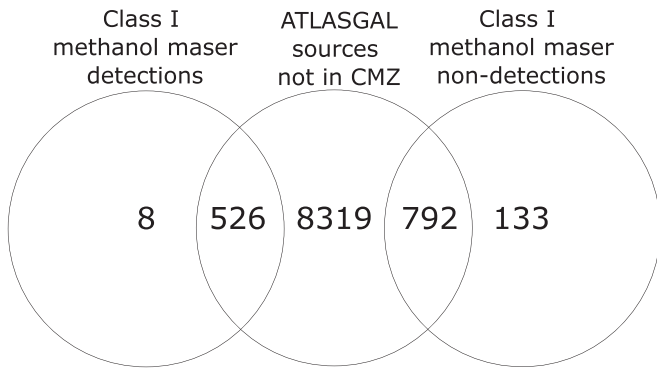


Figure 2. Venn diagram presenting the matching statistics for objects with MMI detections/nondetections and ATLASGAL counterparts in the region $280^\circ < l < 60^\circ$, $|b| < 1.5^\circ$, excluding the CMZ region.

position to the corresponding pixel position on the ATLASGAL masks therefore provides an unambiguous match to the dense clump it is embedded in. We have used these masks as a second independent method to match the ATLASGAL clumps with their embedded masers.

This method eliminates the possibility of a false match caused by an irregular morphology or elongation of the dust emission. However, there is still a possibility for false associations in crowded regions. If many ATLASGAL sources are present near the maser position within the matching radius, then we pick the nearest ATLASGAL clump. Given that most ATLASGAL sources are about $60''$ – $80''$ in size, we can consider that most matches except those made with the Onsala Telescope are reliable to make the correct association between dust clumps and masers. The accuracy of the maser position is essential when considering the cross-match between masers and ATLASGAL sources. The list of masers in the current study uses the interferometric maser positions when possible. Otherwise, the median average of single-dish coordinates is used. That eliminates the significant inaccuracies of maser positions in each maser site. However, when we consider the offsets between dust clumps and maser positions, only interferometric maser positions are used.

We examined the difference in the results of matching obtained using these two methods and this reveals that $\sim 6\%$ of the ATLASGAL counterparts differ. We have visually checked these sources and find that they are mainly localized to crowded regions of ATLASGAL emission where it is difficult to reliably match sources even visually. Given the small number of sources this applies to, we concluded that these sources do not dominate the general statistics. In further analysis, we exclude these sources as being less reliable.

3. Results

3.1. Matching between ATLASGAL and MMI Sources

From the cross-matching between ATLASGAL sources and MMI, we have found that almost 100% of MMI sources are associated with ATLASGAL sources reported in the compact source catalog (Contreras et al. 2013; Urquhart et al. 2014a). The details of the matching statistics are presented in Figure 2. Given that there are ~ 9600 ATLASGAL clumps in the region (excluding the CMZ), the percentage of ATLASGAL sources with known class I counterparts is $\sim 5\%$.

The maser database also stores the MMI nondetections, thus we can study their association with ATLASGAL clumps. From cross-matching using a $60''$ radius, we found that a substantial fraction of objects with a nondetection of MMI (85% of 923 sources) have an ATLASGAL counterpart. Most of them were observed at 95 GHz. That suggests a detection rate toward ATLASGAL sources of $\sim 30\%$.

3.2. Completeness of the Sample of the Detected MMI

To verify the completeness of the sample of the detected MMI sources, we match the data of the blind MMI survey MALT-45 (Jordan et al. 2015) with ATLASGAL data using a $60''$ association radius. This survey has a Galactic coverage of $330^\circ < l < 335^\circ$, $|b| < 0.51^\circ$ and 5σ sensitivity limit of 4.5 Jy. Out of 77 detected MMI, 73 are found to be associated with ATLASGAL clumps, leading to the association rate of 95%.

There are 674 ATLASGAL sources in the region $330^\circ < l < 335^\circ$, $|b| < 0.51^\circ$ and so the MMI association rate with ATLASGAL clumps is 9.8%. Given that the overall match rate is $\sim 5.5\%$ (532 masers in 9646 ATLASGAL sources excluding the CMZ), this might suggest that the Ladeyschikov et al. (2019) MMI catalog only contains $\sim 56\%$ of the total population of masers. This makes a strong case for a new blind survey for MMI or a program of targeted observations toward ATLASGAL sources.

3.3. MMI without ATLASGAL Counterparts

Using the results of the radius-based matching described in Section 3.1 we find associations between 524 MMI and ATLASGAL compact sources within a $60''$ match radius. Given that there are 532 known MMI within the ATLASGAL survey range, this leaves eight MMI ($\sim 1.5\%$) devoid of an associated dust continuum source. Details of these masers are presented in Table 1 and Figure 3.

The sources G331.442–0.158 and G333.818–0.302 are associated with $870 \mu\text{m}$ emission within $12''$. However, the ATLASGAL flux density at the maser position of G333.818–0.302 is only 115 mJy, while $\sigma = 77$ mJy, leading to a detection at the 1.5σ level. Maser G331.442–0.158 appears to be associated with low-level (2 – 3σ) diffuse $870 \mu\text{m}$ emission, which is difficult to separate into sources. Thus these sources were not included in the compact source catalog. Two other sources, G15.094+0.192 and G37.381–0.084, have a weak $870 \mu\text{m}$ compact emission that is below the 3σ detection limit of ATLASGAL, thus they also were not included in the compact source catalog.

The remaining five masers do not have an associated ATLASGAL clump and bright extended emission within a $60''$ radius.

We show all eight sources in Figure 3. Two of the maser sources, G330.828+0.183 and G331.205+0.095, reported by Jordan et al. (2015) were not detected in follow-up observations conducted by Jordan et al. (2017) and so the maser emission may be either spurious detections or variable sources. Thus, only sources G333.772–0.011 and G9.811–1.055 may be considered as detections of MMI without cold dust emission. From multiwavelength analyses, Wide-field Infrared Survey Explorer (WISE) all-sky (Wright et al. 2010), Spitzer IRAC (Fazio et al. 2004), Herschel Photodetector Array Camera and Spectrometer (PACS; Poglitsch et al. 2010), Spectral and Photometric Imaging REceiver (SPIRE; Griffin et al. 2010), and APEX ATLASGAL, of these sources it was found that source G333.772–0.011 with a

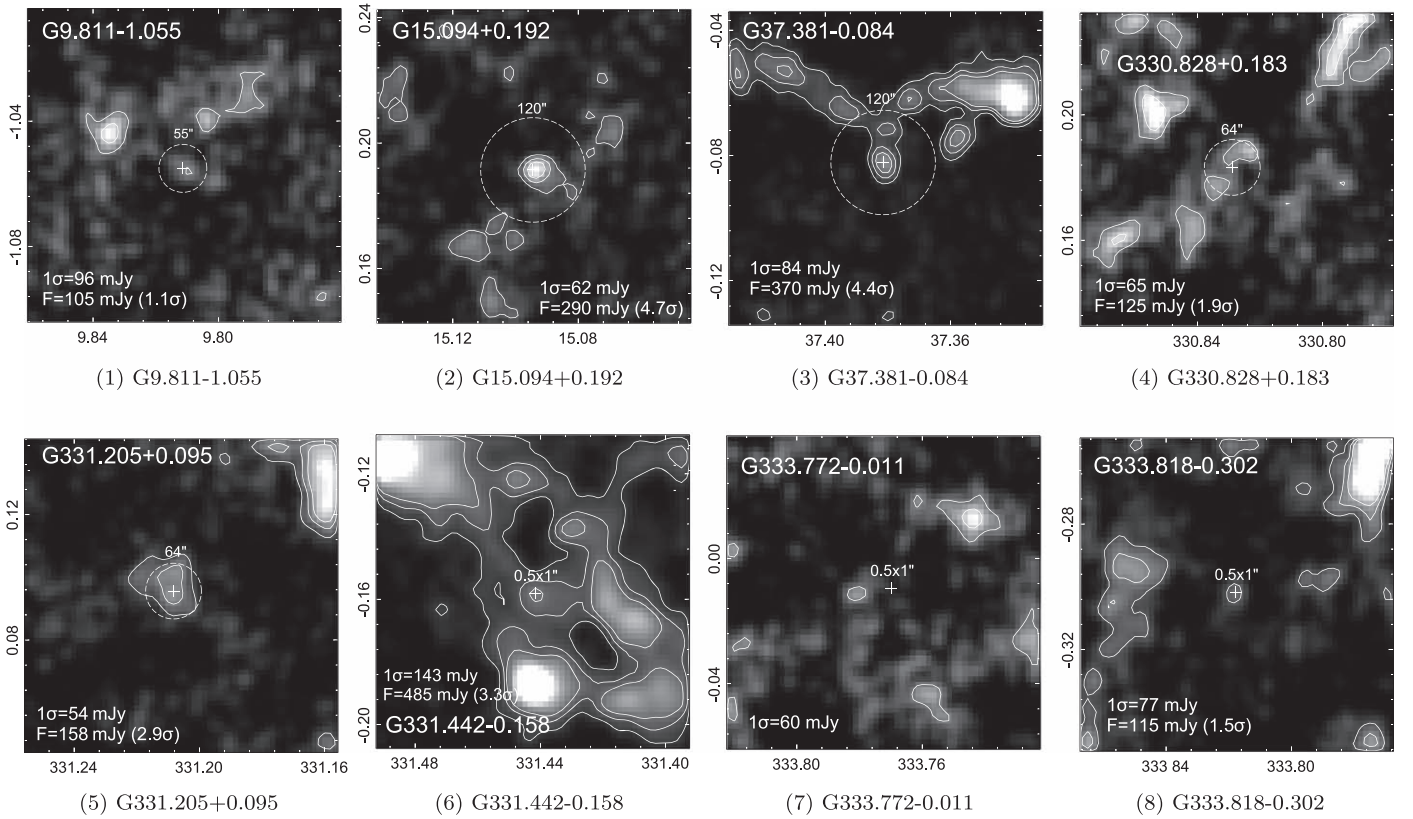


Figure 3. MMI detections without an ATLASGAL compact source counterpart. The coordinate system in each panel is galactic. The background image in each panel is the ATLASGAL $870 \mu\text{m}$ emission. The crosses mark the positions of detected MMI and the circles represent the beam size of the corresponding observations. Contour levels are 1σ , 2σ , and 3σ levels of $870 \mu\text{m}$ emission. In each panel the 1σ level is described together with $870 \mu\text{m}$ flux density at the maser position.

Table 1
List of MMI without Associated ATLASGAL Compact Sources

ID	Source Name	R.A. (h m s)	Decl. (h m s)	$V_{\text{peak}}(\text{MMI})$ (km s^{-1})	$F_{\text{peak}}(\text{MMI})$ (Jy)	$F_{\text{peak}}(870 \mu\text{m})$ (mJy)	References ¹	Notes
1	G9.811–1.055	18 11 19.1	–20 57 56	32.47–34.48	0.93–2.88	105 (96)	YAN17; YAN20	
2	G15.094+0.192	18 17 20.9	–15 43 46	30.36	3.5	290 (62)	KIM18	$870 \mu\text{m}$ emission at 4.7σ
3	G37.381–0.084	18 59 51.6	+03 55 18	56	3.2	370 (84)	KAN15	$870 \mu\text{m}$ emission at 4.4σ
4	G330.828+0.183	16 07 41.1	–51 43 48	–82	3.1	125 (65)	JOR15	Spurious?
5	G331.205+0.095	16 09 52.2	–51 32 19	–67.4	3.5	158 (54)	JOR15	Spurious?
6	G331.442–0.158	16 12 04.8	–51 33 56	–85.98	0.73	485 (143)	JOR17	$870 \mu\text{m}$ emission at 3.3σ
7	G333.772–0.011	16 22 00.5	–49 50 21	–89.33; –89.50	16	<60	JOR15; JOR17	
8	G333.818–0.302	16 23 29.5	–50 00 41	–47.70; –48.50	19	115 (77)	JOR15; JOR17	$870 \mu\text{m}$ emission at 1.5σ

Note. References of MMI detections are as follows: YAN17—Yang et al. (2017), YAN20—Yang et al. (2020) KIM18—Kim et al. (2018), JOR15—Jordan et al. (2015), KAN15—Kang et al. (2015), and JOR17—Jordan et al. (2017).

maser flux density of 16 Jy (Jordan et al. 2015, 2017) is the only example of an MMI without a counterpart in the submillimeter range. G9.811–1.055, with a MMI flux density of 2.88 Jy (Yang et al. 2017), has a counterpart in the Herschel SPIRE $500 \mu\text{m}$ map and an associated green source in Spitzer IRAC map. The origin of these masers without ATLASGAL counterparts is unknown and needs further investigation.

4. Discussion

MMI are associated with the compression and heating of the gas, presumably created by shock waves. The tight correlation between MMI and ATLASGAL sources can be attributed to their

association with SFRs that provide the necessary conditions (e.g., heat, density, and shocks) to produce MMI. Taking into account the analysis of methanol masers without an ATLASGAL counterpart (see Section 3.3), we suggest that in close to 100% of the cases MMI are associated with ATLASGAL dust clumps. However, the detection of dust emission does not guarantee the conditions necessary for masers to be present. In the current paper, we focus only on masers in SFRs and leave the MMI in other types of objects for a future study. The other types of objects include extragalactic MMI (e.g., Chen et al. 2016), masers in the CMZ (Cotton & Yusef-Zadeh 2016), masers in supernova remnants (Pihlström et al. 2014; McEwen et al. 2016), and masers in cloud–cloud collisions (Saliu et al. 2002).

4.1. Physical Parameters of the ATLASGAL Clumps Associated with MMI

We utilize the catalog of ATLASGAL physical clump properties (Urquhart et al. 2018) to study the relationship between the physical parameters of clumps and the detection of MMI. For clump radii and mass, we recalculate the values using 870 μm emission above the FWHM flux contour, similar to Billington et al. (2019). Thus the clump mass is named FWHM clump mass in further analysis. This was done to eliminate the effect of radii overestimation in evolved clumps. As the embedded sources evolve and heat their environment, more of the clump outer envelop becomes detectable, thus more evolved clumps tend to be bigger. However, this is an observational bias and not a real evolutionary trend (Urquhart et al. 2018).

Figure 4 presents the cumulative distributions of the clump physical parameters (F_{peak} , T_{dust} , M_{FWHM} , L_{bol} , $n(\text{H}_2)$, and $L_{\text{bol}}/M_{\text{FWHM}}$) for sources both with associated MMI and those that are devoid of the maser emission. From the analysis of these plots, we conclude that clumps associated with MMI have some preferred regions of parameter space.

We have identified the clump parameters that have an association with 95 GHz masers by fitting Gaussian profiles to the noncumulative histograms of the clump physical parameters. Results of the fit are presented in the Table 2. From analysis of the fits we conclude that the physical parameters of maser-associated clumps peak at larger values compared to the sample of clumps with maser nondetections as well as the whole sample of ATLASGAL clumps. This can be seen in Figure 4 with almost all parameters except the FWHM clump mass being systematically higher than for the unassociated clumps. We note that the sample size for the whole ATLASGAL clump catalog is different for each parameter, as not all clumps have defined values of each physical parameter. The minimum sample size is 5354 sources for M_{FWHM} , $L_{\text{bol}}/M_{\text{FWHM}}$, and $n(\text{H}_2)$ parameters. The decreased sample size associated with the inclusion of only sources with a signal-to-noise ratio (S/N) more than 6 for correct FWHM mass and radii estimation.

The distribution of peak flux densities of ATLASGAL sources (see panel A in Figure 4) reveals a pronounced shift between clumps associated with a 95/44 GHz methanol maser and those with 95 GHz methanol maser observations with nondetections. Due to the lack of information about 44 GHz maser nondetections, we used only 95 GHz maser nondetections. The distribution of ATLASGAL clump peak flux density for sources associated with 95 GHz masers peaks at $\log F_{\text{peak}} = 0.372 \pm 0.013$. In contrast, clumps associated with 95 GHz nondetections peak at $\log F_{\text{peak}} = 0.008 \pm 0.008$. 44 GHz masers have almost identical peak values of flux densities as those detected at 95 GHz (see panel A in Figure 4). A Kolmogorov–Smirnov (KS) test of the peak flux densities of sources with and without detected 95 GHz masers gives a p -value of 1.4×10^{-15} , meaning that the distributions can be considered to be significantly different.

We also found pronounced shifts in bolometric luminosity, number density, and luminosity to the FWHM clump mass ratio for clumps associated with 95 GHz masers in comparison with the nondetections of 95 GHz masers. A KS test gives the p -values of 2.9×10^{-8} , 6.6×10^{-16} , and 4.2×10^{-10} for the luminosity, number density, and luminosity to the FWHM clump mass ratio, respectively. We conclude that the differences in these parameters for detected and nondetected masers are

statistically significant at 3σ , i.e., $p < 0.0013$. The KS test for the dust temperature gives a p -value of 0.004, thus the difference is statistically significant at a 2σ level ($p < 0.005$). In contrast, there is no significant difference in the FWHM clump mass for the different subsamples of maser-associated and nondetected clumps. The KS test gives a p -value of 0.15, thus the null hypothesis about the same distribution cannot be rejected at a 2σ level ($p > 0.005$).

Analysis of the distribution of peak flux and dust temperatures (see left panel of Figure 5) shows that 95 GHz methanol masers tend to arise in warmer sources, with a broad range of dust temperatures ($12 \lesssim T \lesssim 30$ (K) with no clearly preferred temperature within that range). The distribution of clump mass and bolometric luminosity (right panel of Figure 5) indicates that masers tend to arise in more luminous clumps not depending on its mass.

For 84% of 95 GHz masers, the luminosity to mass ratio is between $1 < L_{\text{bol}}/M_{\text{FWHM}} < 100$ (M_{\odot}/L_{\odot}). We analyze the cumulative distribution function of the luminosity to FWHM clump mass ratio (see panel (F) in Figure 4) that is considered to be a good diagnostic of the state of the evolution of star-forming clumps (e.g., Molinari et al. 2008). We additionally plot four evolution types of all ATLASGAL clumps from the classification of Urquhart et al. (2018) in panel (F) of Figure 4. It was found that ATLASGAL clumps associated with masers at 44 and 95 GHz have luminosity to mass ratio values between massive star formation (MSF) clumps and young stellar object (YSO) clump subsamples, mainly associated with MSF clumps (as identified by the rms survey; Lumsden et al. 2013). These two samples are both mid-infrared bright, i.e., associated with a 21–24 μm point source with a flux >2.6 mJy (Urquhart et al. 2018). The difference between these two samples is the presence of MSF tracers in MSF clumps, i.e., radio bright H II regions, massive YSOs, and methanol masers (Urquhart et al. 2014b). Given that a fraction of masers (23%; 84 out of 357) are associated with the YSO clump subsample without MSF tracers (MSF subsample), we conclude that class I masers are formed prior to other tracers of star formation and provide the first evidence of star formation activity. This is consistent with the maser evolutionary diagram in SFRs (Ellingsen et al. 2007; Breen et al. 2010), where class I masers are considered to be the earliest tracer of star formation.

However, the preferred regions in parameter space may reflect a bias in the targeted observations of class I masers. To check this, we consider several samples of methanol maser detections (see Figure 4). The first one is chosen to cover all 44 and 95 GHz maser observations in the ATLASGAL survey ($280^{\circ} < l < 60^{\circ}$, $|b| < 1^{\circ}.5$). The second region ($330^{\circ} < l < 335^{\circ}$, $|b| < 0^{\circ}.5$) is limited to the blind survey of MMI—MALT-45 (Jordan et al. 2015, 2017). The analysis of both distributions leads to the conclusion that both samples give the same results, but a larger sample has a smoother distribution. The KS test for a sample of 44 GHz masers detected in the MALT-45 survey and the full sample of 44 GHz masers reveals that there are no significant differences between all considered parameters of the two maser distributions.

The detection rate for the 44, 84, and 36 GHz masers remains unknown due to small samples of nondetected sources (92, 11, and 36, respectively). However, we can estimate the detection rate of 44 GHz masers using the sample of 307 sources that were observed at both 44 and 95 GHz. Of that sample, 271 sources were detected at 95 GHz and 253 were detected at

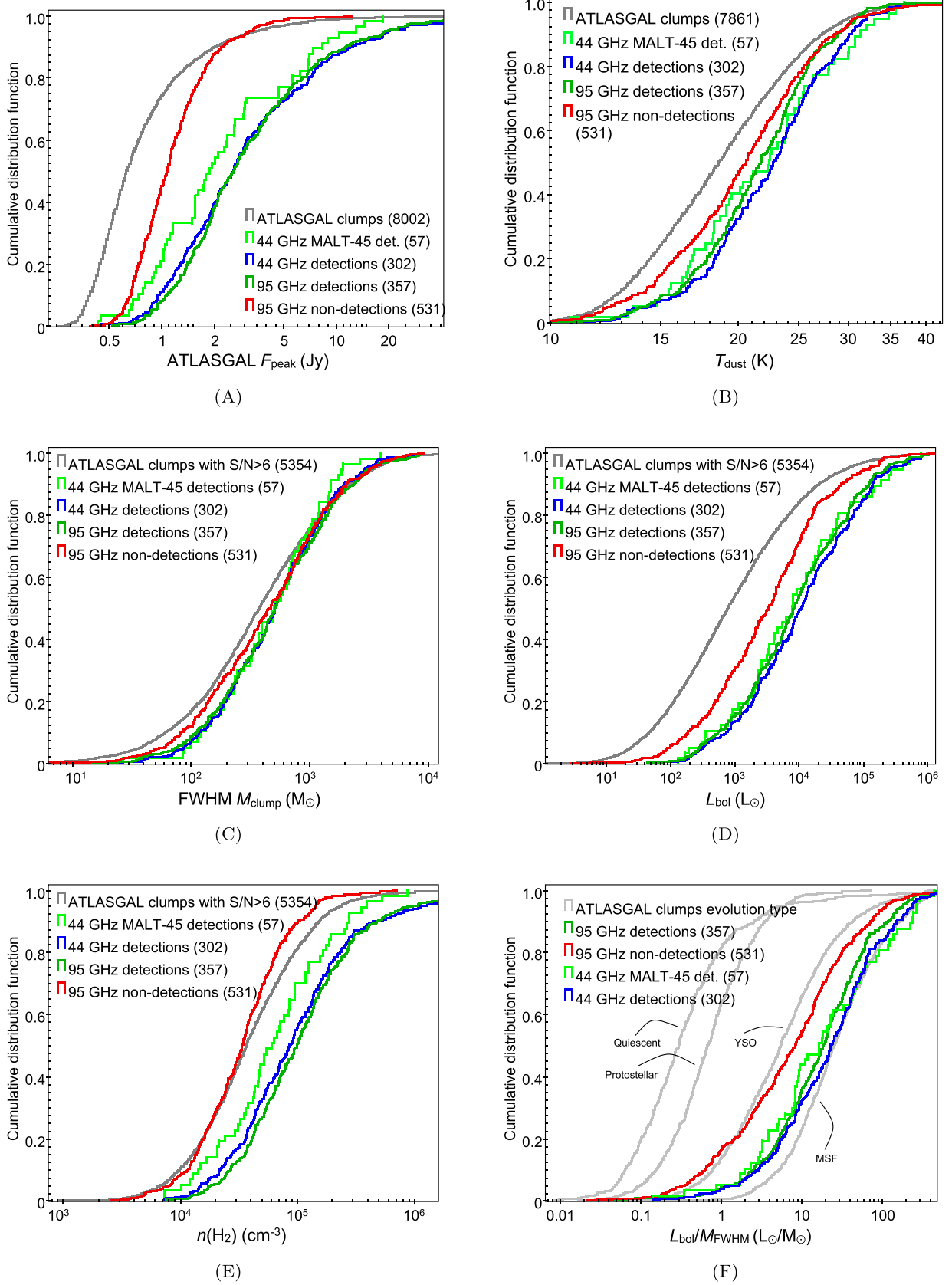


Figure 4. Cumulative distribution plots of clump physical parameters ((A) peak flux density, (B) dust temperature, (C) FWHM mass, (D) bolometric luminosity, (E) number density, and (F) luminosity to clump mass ratio) associated with MMI. The gray line shows all ATLASGAL sources ($280^{\circ} < l < 60^{\circ}$, $|b| < 1.5^{\circ}$) with defined parameters. The green and red lines show those ATLASGAL clumps with an observed detection and nondetection of 95 GHz masers, respectively. The blue line is maser-associated clumps at 44 GHz. The light green line shows the sources with 44 GHz masers detected in the MALT-45 survey (Jordan et al. 2015; $330 < l < 335$, $|b| < 0.5^{\circ}$). In the last panel (F) gray lines show the different evolution types of all ATLASGAL sources, marked with labels.

Table 2

Peak Values from the Gaussian Fit of the Clump Physical Parameter Histograms in Three Samples: ATLASGAL Clumps Associated with Masers at 95 GHz, ATLASGAL Clumps with No Class I Maser Detection at 95 GHz, and the Full Sample of ATLASGAL Clumps with Available Physical Parameters

Sample Size	With Maser 442	No Maser 703	All Clumps 8002
$\log F_{\text{peak}}$	0.372 ± 0.013 < 0.11 >	0.008 ± 0.008 < 0.07 >	-0.245 ± 0.007 < 0.08 >
$\log N_{\text{H}_2}$	22.784 ± 0.013 < 0.12 >	22.442 ± 0.009 < 0.08 >	22.28 ± 0.005 < 0.04 >
$\log L_{\text{bol}}$	3.905 ± 0.038 < 0.07 >	3.382 ± 0.035 < 0.08 >	2.868 ± 0.018 < 0.03 >
$\log T_{\text{dust}}$	1.339 ± 0.005 < 0.9 >	1.313 ± 0.003 < 0.07 >	1.268 ± 0.002 < 0.05 >
$\log M_{\text{FWHM}}$	2.714 ± 0.033 < 0.04 >	2.657 ± 0.028 < 0.04 >	2.587 ± 0.013 < 0.01 >
$\log n(\text{H}_2)$	4.958 ± 0.016 < 0.09 >	4.519 ± 0.016 < 0.06 >	4.564 ± 0.008 < 0.03 >
$\log L_{\text{bol}}/M_{\text{FWHM}}$	1.281 ± 0.911 < 0.09 >	0.023 ± 0.022 < 0.09 >	0.65 ± 0.013 < 0.05 >

Note. The estimation of the parameter errors are shown after the \pm symbol. Values in brackets are the standard deviation of the Gaussian fit.

44 GHz. Thus, the detection rates are comparable for both frequencies, and we assume that the sample of 44 GHz nondetected sources are similar to the nondetected at 95 GHz.

From analysis of the physical parameters of clumps associated with MMI at 95 and 44 GHz, we conclude that masers tend to arise in more luminous clumps with higher densities (both column density and number density) and temperatures compared to the full sample of the ATLASGAL clumps. This is likely because protostars are associated with warmer and higher luminosity clumps and these are the sources that produce the shocks conducive to MMI emission. Furthermore, clumps associated with masers may be more heavily influenced by shocks than those devoid of masers and, hence, their average densities, luminosities, and temperatures are all higher.

Shock wave propagation in clumps with higher densities and temperatures has a higher potential to increase densities and temperatures to the levels required for efficient MMI pumping. Clumps with higher luminosities have higher column densities, increasing the probability of acquiring high methanol column density in the shocked region, which is necessary to produce bright masers. The lower detection rates in very luminous and hot objects is likely because these objects have already evolved into H II regions and have already started to disrupt their environments. However, MMI may arise even further while the H II region begins to expand and create the density waves with appropriate conditions (mainly density and temperature).

4.2. Separation between Methanol Masers and ATLASGAL Clumps

We have limited our analysis of MMI and MMII offsets from ATLASGAL clump peaks to the sample of masers with interferometric positions as listed in the maser database (Ladeyschikov et al. 2019). In cases where many maser spots are detected in a particular observation, we consider the brightest maser spot as the position for that group. In cases where several

interferometric observations are available for a source, we select the median mean value of the available positions. The physical distances to the sources were taken from Urquhart et al. (2018). We use a distance-limited sample in a range of 1–6 kpc to avoid any distance bias (see panel (A) in Figure 6). The positions of the brightest maser spots were matched with the ATLASGAL catalog using 30'' matching radius, resulting in 153 matches for MMI and 374 matches for MMII for the distance-limited sample. The results are presented in panel (B) of Figure 6 in the form of the cumulative distribution of offsets between ATLASGAL clump peak and position of MMI and MMII. It shows the physical separation between ATLASGAL clump peak position and interferometric positions of MMI and MMII.

The collisional–radiative pumping of MMI should impact the linear separation between host dust clumps and positions of these masers. In contrast, the MMII at 6.7 GHz are pumped by infrared radiation and reside in the circumstellar disks and inner parts of the outflows of high-mass YSOs, which have sizes less than 1000 au (Sanna et al. 2015, 2017). The characteristic scale of the MMI distribution is about 50 times larger (e.g., Voronkov et al. 2014). Thus positions of MMII can be regarded as the YSO position. The panel (B) of Figure 6 clearly shows that there is a physical separation between ATLASGAL clumps and MMI and MMII, with MMI being located at larger distances from the ATLASGAL clumps than the MMII. This is in accord with the current understanding of the methanol maser origin and results of the previous analysis given in, e.g., Voronkov et al. (2014). While the MMII are radiatively pumped in the accreting disk, the MMI are pumped by shocks and can be located further from the embedded protostar. The mean distances between ATLASGAL clumps and methanol masers are found to be 0.16 and 0.11 pc for MMI and MMII, respectively.

A KS test comparing the offsets of the two methanol maser classes located between 1 and 6 kpc gives a p -value $\ll 0.0013$, confirming that the distributions of MMI and MMII within a clump are statistically significantly different.

4.3. Correlation between MMI Fluxes and ATLASGAL Clump Parameters

We investigated the correlation between maser luminosity and ATLASGAL clump physical parameters by utilizing the nonparametric partial Spearman’s correlation coefficients, which remove the mutual dependence on the distance. We derive Spearman’s correlation coefficients for each of the groups in two different samples—full and distance-limited ($1 < D < 6$ kpc), as the maser flux for distant objects is limited by the telescope sensitivity, thus maser luminosity (as well as clump physical size) have higher uncertainty. The maser isotropic luminosity (hereafter luminosity) is calculated using $L_{\text{maser}} = 4\pi D^2 F_{\text{maser}}$, where D is the distance from Urquhart et al. (2018). The results of the correlation analysis are presented in Table 3.

Analysis of the correlation coefficients has revealed that the maximum correlation in a full sample of maser-associated clumps ($N = 357$) is found between the maser luminosity and the FWHM clump mass ($r = 0.46$), as well as bolometric luminosity ($r = 0.4$). However, the number density has a low correlation with maser luminosity in a full sample of maser-associated clumps. That can be due to uncertainty in the mass and radius estimations for distant objects. In the distance-limited sample ($1 < D < 6$ kpc), number density along with

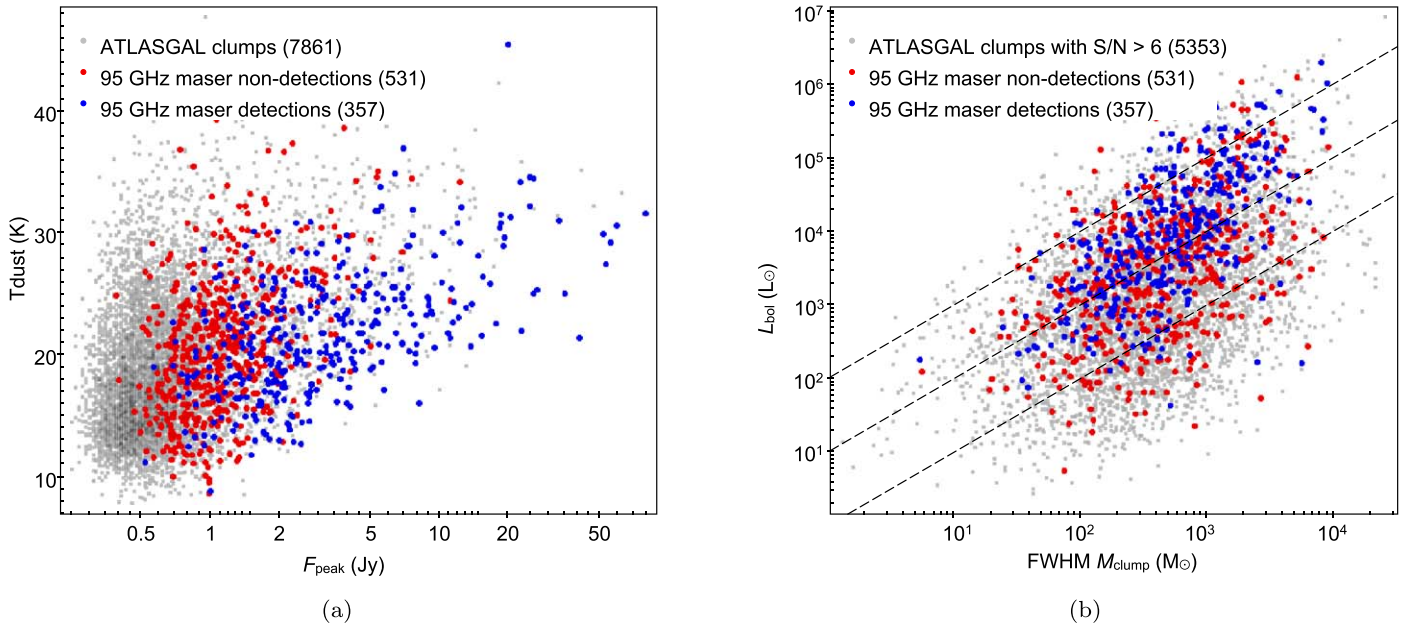


Figure 5. Distribution of ATLASGAL clumps peak flux density, dust temperature, luminosity, and FWHM mass for all ATLASGAL clumps (gray dots), clumps associated with 95 GHz masers (blue dots), and clumps with nondetection of 95 GHz masers (red dots). Lower, middle, and upper diagonal lines indicate the $L_{\text{bol}}/M_{\text{clump}} = 1, 10$ and $100 L_{\odot}/M_{\odot}$, respectively.

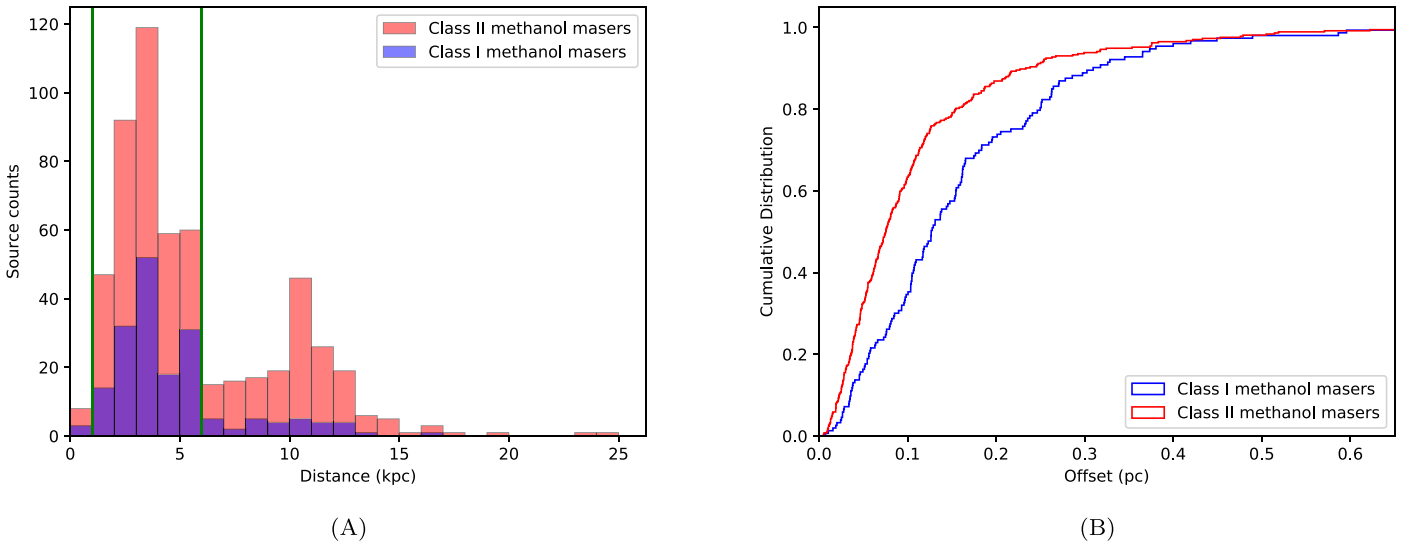


Figure 6. (A) Distribution of the distances to detected MMI and MMII. The green vertical line marks the distance-limited sample used for the construction of the cumulative offsets plot. (B) Cumulative distribution of the physical offsets between the ATLASGAL clump peak and methanol maser positions from the interferometric observations of a distance-limited sample ($1 < D < 6$ kpc).

other parameters reveal almost similar correlations with $r \simeq 0.3$ – 0.4 . We conclude that more luminous, dense, and massive clumps tend to produce more luminous masers.

In Figure 7 we present the log–log plot of ATLASGAL $870 \mu\text{m}$ flux density against 95 GHz maser peak flux density. The correlation analysis for these two parameters gives the correlation coefficient $r = 0.4$, similar to other parameters (see Table 3). From a linear fit in log–log space we obtain the following power-law relation $F_{\text{maser}} = F_{\text{ATLASGAL}}^{0.472 \pm 0.004} \times 10^{0.661 \pm 0.003}$, where F_{maser} and F_{ATLASGAL} both have units of Jy. The scatter in the data is quite significant ($\sigma[\log F_{\text{maser}}] = 0.41$) and so we are unable to assign a particular value of maser flux density from the ATLASGAL peak flux density. However, in a distance-limited sample we find no masers below the 2σ level that have peak flux

densities lower than predicted by the ATLASGAL peak flux density. Thus the empirical equation for the lower estimate of 95 GHz maser peak flux density can be written as

$$F_{95 \text{ GHz, lower}} = F_{\text{ATLASGAL}}^{0.472} \times 10^{0.661 - 2\sigma}, \quad (1)$$

where $\sigma = 0.41$, and $F_{95 \text{ GHz}}$ and F_{ATLASGAL} are the peak flux densities (in Jy) of 95 GHz masers and ATLASGAL sources, respectively. This equation may be used to estimate the minimum required noise level to detect 95 GHz methanol maser in a particular ATLASGAL source. In a distance-limited sample 100% of masers have 95 GHz peak flux densities higher than the value determined from Equation (1), and in a full sample it is 99% of the masers.

Table 3Partial Correlation Coefficients (r) between 95 GHz Maser Luminosities and ATLASGAL Clumps Physical Parameters

Parameter	Sample	r	N	p -value
$\log[T_{\text{dust}}]$	Full	0.19 [0.09, 0.29]	357	0.027
	Limited	0.24 [0.12, 0.35]	265	$\ll 0.001$
$\log[L_{\text{bol}}]$	Full	0.40 [0.31, 0.48]	357	$\ll 0.001$
	Limited	0.39 [0.28, 0.49]	265	$\ll 0.001$
$\log[M_{\text{FWHM}}]$	Full	0.46 [0.37, 0.53]	357	$\ll 0.001$
	Limited	0.37 [0.26, 0.47]	265	$\ll 0.001$
$\log[N(\text{H}_2)]$	Full	0.28 [0.18, 0.37]	357	$\ll 0.001$
	Limited	0.41 [0.30, 0.50]	265	$\ll 0.001$
$\log[L/M_{\text{FWHM}}]$	Full	0.22 [0.12, 0.31]	357	$\ll 0.001$
	Limited	0.28 [0.16, 0.39]	265	$\ll 0.001$
$\log[n(\text{H}_2)]$	Full	0.12 [0.02, 0.22]	357	0.02
	Limited	0.31 [0.20, 0.42]	265	$\ll 0.001$

Note. Values in the brackets are the 95% correlation confidence intervals. N is the sample size, and p -value is the significance of the correlations. Limited refers to the distance-limited sample of ATLASGAL clumps within $1 < D < 6$ kpc.

4.4. Using ATLASGAL to Search for MMI

We investigate the potential to use a subset of the ATLASGAL compact source catalog as a target list for further searches of MMI. As previously mentioned in Section 3.2, the MALT-45 blind survey reveals an MMI association rate with ATLASGAL sources of 95% and the association of $\sim 10\%$ of ATLASGAL sources with MMI. The MALT-45 survey has a median noise level of 0.90 ± 0.09 Jy for 44 GHz MMI.

The total number of ATLASGAL sources is much larger than the number of detected MMI. To use the ATLASGAL compact source catalog efficiently for targeted observations, we need to develop a set of robust selection criteria that will maximize the detection rate.

In the first approach, we investigate the possibility of using the threshold on $870 \mu\text{m}$ peak flux density of ATLASGAL sources for selecting the clumps with a high maser detection rate. As was shown in Table 2, there is a pronounced shift between flux density and H_2 column density of the detected and nondetected samples. Thus, the threshold on the ATLASGAL source peak flux density or H_2 column density may significantly increase the detection rate, but miss a fraction of low-brightness ATLASGAL clumps associated with masers. To avoid this and cover at least 96% of detected masers associated with ATLASGAL clumps we have used either of the following thresholds:

$$F_{\text{peak}} > 0.85 \text{ Jy} \quad (2)$$

$$\log N(\text{H}_2) > 22.3 \text{ cm}^{-2}. \quad (3)$$

The analysis of Equation (2) lead to the conclusion that the 95 GHz maser detection rate toward ATLASGAL sources satisfying that criteria is $\sim 50\%$ for an available sample of 784 objects. The typical σ level for achieving this detection rate is 0.2 Jy. The same analysis for Equation (3) lead to the detection rate of $\sim 45\%$ for the sample of 793 objects.

A similar analysis of the Bolocam Galactic Plane Survey (BGPS) with sources satisfying $\log(S_{\text{int}}) \leq -38.0 + 1.72 \log(N_{\text{H}_2}^{\text{beam}})$ and $\log(N_{\text{H}_2}^{\text{beam}}) \geq 22.1$ (Chen et al. 2012) lead to the detection rate of 30% with a sample of ~ 1000 sources. This value is close to the observed detection rate of 29% (Chen et al. 2012) with a sample of 214 sources.

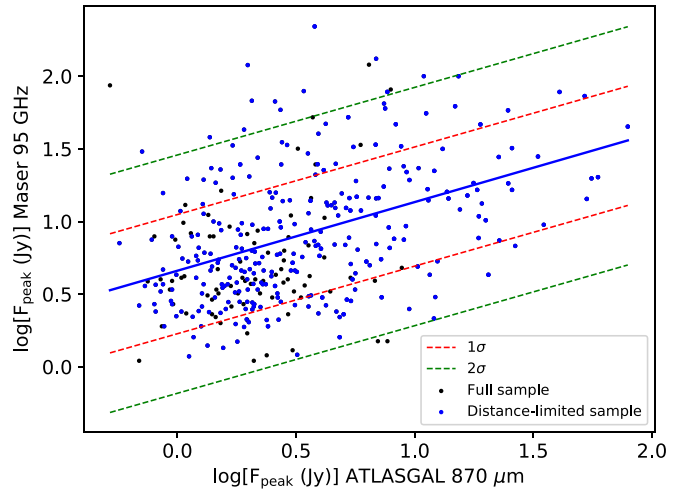


Figure 7. Distribution of ATLASGAL peak flux density against the 95 GHz masers peak flux density. Black points and line refer to a full sample of maser-associated clumps, and the blue points and line refer to a distance-limited sample ($1 < D < 6$ kpc). The solid blue line is the linear fit (power law in a log-scale) to the distance-limited sample. Red and green dashed lines are 1σ and 2σ level of the deviation around the fit.

5. Conclusions

From the analysis of MMI and ATLASGAL sources, we have found a tight physical correlation between them—almost 100% of MMI sources have ATLASGAL counterparts. Analysis of the physical parameters of maser-associated ATLASGAL clumps leads to the following conclusions.

1. The distribution of ATLASGAL clumps that have been the targets of methanol maser observations reveals statistically significant differences in physical parameters between 95/44 GHz maser-associated clumps and ATLASGAL clumps without the detection of 95 GHz masers. The following parameters have statistically significant difference: peak flux density, number density, column density, bolometric luminosity, luminosity to clump mass ratio, and dust temperature.
2. Masers tend to arise in more luminous clumps with higher densities and slightly higher temperatures (significant at the 2σ level) compared to the whole sample of the ATLASGAL clumps. We conclude that the warmer and higher luminosity clumps host protostars and it is the shocks they generate that drive the masers. From the analysis of partial correlation coefficients between 95 GHz maser luminosities and ATLASGAL clump physical parameters, we conclude that more luminous, dense, and massive clumps tend to produce more bright masers.
3. Of the 95 GHz masers 23% (84 out of 357) are associated with ATLASGAL clumps that are mid-infrared bright, i.e., associated with a 21–24 μm point source with a flux > 2.6 mJy (Urquhart et al. 2018), but display no other tracers of massive star formation, i.e., radio bright H II regions, massive YSO, or MMII (Urquhart et al. 2014b). This leads us to conclude that MMI are formed prior to other tracers of star formation and provide the first evidence of star formation activity. This is consistent with the maser evolutionary diagram in SFRs (Ellingsen et al. 2007; Breen et al. 2010), where MMI are some of the earliest tracers of star formation.

4. The physical separation between the center of the clumps and the brightest maser spots is significantly smaller for MMII compared to MMI. This is consistent with our understanding of the pumping mechanisms and their connection with the star formation process—the MMII are radiatively pumped in the accreting disk, but the MMI are pumped by shocks and can be located further from the embedded protostar. The mean distances between ATLASGAL clumps and methanol masers are found to be 0.16 and 0.11 pc for MMI and MMII, respectively.
5. We investigate the potential of the ATLASGAL compact source catalog as a target list for the search of MMI. The threshold values of $F_{\text{ATLASGAL}} > 0.85$ Jy or $\log N(\text{H}_2) > 22.3 \text{ cm}^{-2}$ give a coverage of 95% known MMI with estimated detection rate of $\sim 50\%$ at 1σ level of ~ 0.2 Jy for maser observations.

The work of D.A.L. in the Section 3 was supported by the Ministry of Education and Science of Russia (the basic part of the State assignment, RK no. FEUS-2020-0030). The work of D.A.L. and A.M.S. in the Section 4.1 was supported by Russian Science Foundation grant 18-12-00193. The work of D.A.L. in the Sections 4.2–4.4 were supported by Russian Foundation for Basic Research through research project 18-32-00605.

ORCID iDs

Dmitry A. Ladeyschikov  <https://orcid.org/0000-0002-3773-7116>

James S. Urquhart  <https://orcid.org/0000-0002-1605-8050>

Shari L. Breen  <https://orcid.org/0000-0002-4047-0002>

Olga S. Bayandina  <https://orcid.org/0000-0003-4116-4426>

References

- Aguirre, J. E., Ginsburg, A. G., Dunham, M. K., et al. 2011, *ApJS*, **192**, 4
- Bae, J.-H., Kim, K.-T., Youn, S.-Y., et al. 2011, *ApJS*, **196**, 21
- Batrla, W., Matthews, H. E., Menten, K. M., & Walmsley, C. M. 1987, *Natur*, **326**, 49
- Bertin, E., & Amouts, S. 1996, *A&AS*, **117**, 393
- Billington, S. J., Urquhart, J. S., König, C., et al. 2019, *MNRAS*, **490**, 2779
- Breen, S. L., Contreras, Y., Dawson, J. R., et al. 2019, *MNRAS*, **484**, 5072
- Breen, S. L., Ellingsen, S. P., Caswell, J. L., & Lewis, B. E. 2010, *MNRAS*, **401**, 2219
- Breen, S. L., Fuller, G. A., Caswell, J. L., et al. 2015, *MNRAS*, **450**, 4109
- Caswell, J. L., Fuller, G. A., Green, J. A., et al. 2010, *MNRAS*, **404**, 1029
- Caswell, J. L., Fuller, G. A., Green, J. A., et al. 2011, *MNRAS*, **417**, 1964
- Chen, X., Ellingsen, S. P., He, J.-H., et al. 2012, *ApJS*, **200**, 5
- Chen, X., Ellingsen, S. P., Shen, Z.-Q., Titmarsh, A., & Gan, C.-G. 2011, *ApJS*, **196**, 9
- Chen, X., Ellingsen, S. P., Zhang, J. S., et al. 2016, *MNRAS*, **459**, 357
- Contreras, Y., Schuller, F., Urquhart, J. S., et al. 2013, *A&A*, **549**, A45
- Cotton, W. D., & Yusef-Zadeh, F. 2016, *ApJS*, **227**, 10
- Cragg, D. M., Sobolev, A. M., & Godfrey, P. D. 2005, *MNRAS*, **360**, 533
- Dunham, M. K., Robitaille, T. P., Evans, N. J. I., et al. 2011, *ApJ*, **731**, 90
- Eden, D. J., Moore, T. J. T., Plume, R., et al. 2017, *MNRAS*, **469**, 2163
- Ellingsen, S. P., Voronkov, M. A., Cragg, D. M., et al. 2007, in IAU Symp. 242, *Astrophysical Masers and their Environments*, ed. J. M. Chapman & W. A. Baan (Cambridge: Cambridge Univ. Press), 213
- Fazio, G. G., Hora, J. L., Allen, L. E., et al. 2004, *ApJS*, **154**, 10
- Gan, C.-G., Chen, X., Shen, Z.-Q., Xu, Y., & Ju, B.-G. 2013, *ApJ*, **763**, 2
- Green, J. A., Caswell, J. L., Fuller, G. A., et al. 2010, *MNRAS*, **409**, 913
- Green, J. A., Caswell, J. L., Fuller, G. A., et al. 2012, *MNRAS*, **420**, 3108
- Griffin, M. J., Abergel, A., Abreu, A., et al. 2010, *A&A*, **518**, L3
- Jordan, C. H., Walsh, A. J., Breen, S. L., et al. 2017, *MNRAS*, **471**, 3915
- Jordan, C. H., Walsh, A. J., Lowe, V., et al. 2015, *MNRAS*, **448**, 2344
- Kalenskii, S. V., Kurtz, S., & Bergman, P. 2013, *ARep*, **57**, 120
- Kang, H., Kim, K.-T., Byun, D.-Y., Lee, S., & Park, Y.-S. 2015, *ApJS*, **221**, 6
- Kim, C.-H., Kim, K.-T., & Park, Y.-S. 2018, *ApJS*, **236**, 31
- Kim, W.-J., Kim, K.-T., & Kim, K.-T. 2019, *ApJS*, **244**, 2
- Ladeyschikov, D. A., Bayandina, O. S., & Sobolev, A. M. 2019, *AJ*, **158**, 233
- Leurini, S., & Menten, K. M. 2018, in IAU Symp. 336, *Astrophysical Masers: Unlocking the Mysteries of the Universe*, ed. A. Tarchi, M. J. Reid, & P. Castangia (Cambridge: Cambridge Univ. Press), 17
- Lumsden, S. L., Hoare, M. G., Urquhart, J. S., et al. 2013, *ApJS*, **208**, 11
- McEwen, B. C., Pihlström, Y. M., & Sjouwerman, L. O. 2016, *ApJ*, **826**, 189
- Menten, K. M. 1991, *ApJL*, **380**, L75
- Molinari, S., Pezzuto, S., Cesaroni, R., et al. 2008, *A&A*, **481**, 345
- Moore, T. J. T., Plume, R., Thompson, M. A., et al. 2015, *MNRAS*, **453**, 4264
- Pihlström, Y. M., Sjouwerman, L. O., Frail, D. A., et al. 2014, *AJ*, **147**, 73
- Poglitsch, A., Waelkens, C., Geis, N., et al. 2010, *A&A*, **518**, L2
- Salii, S. V., Sobolev, A. M., & Kalinina, N. D. 2002, *ARep*, **46**, 955
- Sanna, A., Moscadelli, L., Surcis, G., et al. 2017, *A&A*, **603**, A94
- Sanna, A., Surcis, G., Moscadelli, L., et al. 2015, *A&A*, **583**, L3
- Schuller, F., Menten, K. M., Contreras, Y., et al. 2009, *A&A*, **504**, 415
- Sobolev, A. M., Cragg, D. M., Ellingsen, S. P., et al. 2007, in IAU Symposium, Vol. 242, *Astrophysical Masers and their Environments*, ed. J. M. Chapman & W. A. Baan (Cambridge: Cambridge Univ. Press), 81
- Sobolev, A. M., & Parfenov, S. Y. 2018, in IAU Symp. 336, *Astrophysical Masers: Unlocking the Mysteries of the Universe*, ed. A. Tarchi, M. J. Reid, & P. Castangia (Cambridge: Cambridge Univ. Press), 57
- Urquhart, J. S., Csengeri, T., Wyrowski, F., et al. 2014a, *A&A*, **568**, A41
- Urquhart, J. S., König, C., Giannetti, A., et al. 2018, *MNRAS*, **473**, 1059
- Urquhart, J. S., Moore, T. J. T., Csengeri, T., et al. 2014b, *MNRAS*, **443**, 1555
- Urquhart, J. S., Moore, T. J. T., Menten, K. M., et al. 2015, *MNRAS*, **446**, 3461
- Urquhart, J. S., Moore, T. J. T., Schuller, F., et al. 2013, *MNRAS*, **431**, 1752
- Val'ts, I. E., Ellingsen, S. P., Slysh, V. I., et al. 2020, *MNRAS*, **317**, 315
- Voronkov, M. A., Brooks, K. J., Sobolev, A. M., et al. 2006, *MNRAS*, **373**, 411
- Voronkov, M. A., Caswell, J. L., Ellingsen, S. P., Green, J. A., & Breen, S. L. 2014, *MNRAS*, **439**, 2584
- Voronkov, M. A., Caswell, J. L., Ellingsen, S. P., & Sobolev, A. M. 2010, *MNRAS*, **405**, 2471
- Wright, E. L., Eisenhardt, P. R. M., Mainzer, A. K., et al. 2010, *AJ*, **140**, 1868
- Yang, W., Xu, Y., Chen, X., et al. 2017, *ApJS*, **231**, 20
- Yang, W., Xu, Y., Choi, Y. K., et al. 2020, *ApJS*, **248**, 18